

1 **Application of subject-specific adaptive mechanical loading for bone**
2 **healing in a mouse tail vertebral defect.**

3

4

5 Angad Malhotra¹, Matthias Walle¹, Graeme R. Paul¹, Gisela A. Kuhn¹, Ralph Müller^{1*}.

6 ¹Institute for Biomechanics, ETH Zurich, Zurich, Switzerland.

7

8

9

10 ***Corresponding author:**

11 Ralph Müller, PhD

12 Institute for Biomechanics

13 ETH Zurich

14 Leopold-Ruzicka-Weg 4

15 8093 Zurich, Switzerland

16 Email: ram@ethz.ch

17 **Abstract**

18 Methods to repair bone defects arising from trauma, resection, or disease, continue to be sought after.
19 Cyclic mechanical loading is well established to influence bone (re)modelling activity, in which bone
20 formation and resorption are correlated to micro-scale strain. Based on this, the application of
21 mechanical stimulation across a bone defect could improve healing. However, if ignoring the
22 mechanical integrity of defected bone, loading regimes have a high potential to either cause damage or
23 be ineffective. This study explores real-time finite element (rtFE) methods that use three-dimensional
24 structural analyses from micro-computed tomography images to estimate effective peak cyclic loads in
25 a subject-specific and time-dependent manner. It demonstrates the concept in a cyclically loaded
26 mouse caudal vertebral bone defect model. Using rtFE analysis combined with adaptive mechanical
27 loading, mouse bone healing was significantly improved over non-loaded controls, with no incidence
28 of vertebral fractures. Such rtFE-driven adaptive loading regimes demonstrated here could be relevant
29 to clinical bone defect healing scenarios, where mechanical loading can become patient-specific and
30 more efficacious. This is achieved by accounting for initial bone defect conditions and spatio-temporal
31 healing, both being factors that are always unique to the patient.

32 **Introduction**

33 The management of critical-size bone defects continues to present surgical challenges. Trauma and
34 bone resection can lead to lengthy recovery times or amputation. The use of autografts is the current
35 gold standard, however, is quantity-limited and accounts for 20% of the complications¹. Despite
36 advances in biomaterial development and understanding of signaling mechanisms, the search for
37 improved treatment methods of such bone defects continues.

38

39 One treatment method of interest is mechanical loading of bone. Mechanical interactions have a long-
40 established relationship to bone physiology, leading to earlier concepts of micromotion during bone
41 defect healing², and the significance of fracture instability in healing outcomes^{3,4}. The effects of
42 mechanical forces on bone healing have been previously reviewed^{5,6}; mechanical loading is likely to
43 depend on frequency⁷ and cycle number⁸, influences mesenchymal stem cell differentiation⁹, and has a
44 role in guiding healing towards primary and secondary bone healing pathways¹⁰. In contrast,
45 mechanical loading and relative motion of fragments showed little to no benefit in other studies^{11,12},
46 though the timing of the changes of the mechanical environment in relation to healing phases could
47 also play a role¹³. This further highlights the need to understand the mechanical environment in and
48 around bone defects during healing. This mechanical environment of bone includes the relevant
49 surrounding hard and soft tissues, and their interaction as subject to Newtonian mechanics, which
50 allows computational exploitation for assessing the loading history and relationship to morphological
51 changes¹⁴. However, the translation of these load-driven bone (re)modelling concepts to highly unique
52 bone defect healing scenarios is lacking. Another current challenge that arises is how to determine the
53 force that needs to be applied in a subject-specific manner in order to have a maximal
54 mechanobiological cue without damaging the bone.

55

56 Finite element (FE) analysis is a well-proven approach to understand micro-scale strains and has been
57 previously successfully used to correlate strain and in vivo bone (re)modelling activities in mice¹⁵⁻¹⁷.
58 In such workflows, bone mechanoregulation can be studied non-invasively by combining imaging and

59 computational FE-derived strain estimation methods¹⁸. With advances in computational power, the
60 time needed to calculate voxel-based strains relevant for bone healing has drastically shortened in the
61 last decade. Depending on the complexity and resolution deemed suitable, it is possible to do this
62 immediately after imaging to limit unnecessary or additional handling and anesthesia in mice. This
63 concept is concurrently presented in a mouse femoral defect model^{19,20}, and in combination introduce
64 the concept of real-time finite element (rtFE) analysis to describe this approach. Since mechanical
65 loading is effective only within a certain strain window²¹, maintaining the applied loading within this
66 window is critical. Loading too high risks damage (Supplementary Fig. S1a) and loading too low risks
67 no effect. FE analysis can be used to estimate the optimal forces, and the rtFE method builds on this
68 by streamlining the process of imaging, analysis, and treatment.

69

70 Two factors are relevant for determination of the appropriate loading conditions: the defect itself; and
71 its changes due to healing. First, every defect is unique in shape, size, and location. This, in
72 combination with the surrounding structural anatomy, will influence how strain is transferred across
73 the region. Second, inherent differences between an individual's healing capabilities will always exist.
74 When bone heals, the tissue-level stiffness increases. If constant stimuli are applied, micro-level
75 strains will decrease as bone forms and reinforces the defect. This would lead to a lowering of the
76 regional strain, and result in sub-optimal loading conditions. Therefore, applying individualized and
77 adapting loading regimes that factor in the defect and its unique healing has high potential to promote
78 bone healing, not only in mice, but in humans, where these two factors can vary widely case to case.

79

80 Applying loads to a bone defect, and imaging it at the necessary resolution, are fundamental
81 requirements of this study. A previously described method enabled the loading of mouse vertebrae²²⁻
82 ²⁴, and importantly, allowed high-resolution scanning of the vertebrae. This was recently advanced on
83 to investigate the loading frequency effect on mouse vertebral bone parameters²⁵. To investigate
84 specifically bone defect healing in this current study, a caudal vertebral bone defect model was
85 developed, which could be incorporated into the previously successfully used workflows. This model

86 is straightforward, reproducible and facilitates biomaterial placement²⁶. In comparison to commonly
87 used mouse hind leg models, the vertebral model can reduce the complexity and uncertainty within the
88 FE simulation. For example, hind leg models can have more complex boundary conditions due to
89 more complex joint constraints of the limb, greater influence from external bodyweight loadings due
90 to gravity, and higher internal muscle-bone loads applied by the mouse during ambulation²⁷.
91 Furthermore, the vertebral model requires no surgical fixation, and allows for early loading post-
92 surgery due to the high initial stability of the defect region compared to osteotomy-based models. This
93 lack or presence of fixation can make comparisons difficult, even if one considers that the
94 mechanobiological responses are consistent. Overall, the vertebral defect model introduced here
95 provides another anatomical location to advance theories of bone mechanoregulation during defect
96 healing.

97

98 Longitudinal time-lapsed imaging with micro-computed tomography (micro-CT) is a suitable method
99 to image bone at the early stages of healing²⁸. This can provide short time interval snapshots of the
100 healing progression and create high-resolution datasets for FE simulations. This time-lapsed imaging
101 method is currently most feasible in smaller animals, and has been previously demonstrated in
102 vertebrae²², and recently within both mouse femoral defect models²⁹, and to assess longer-term
103 morphological changes of intact mouse vertebrae^{25,30}. This method is highly relevant here to provide
104 weekly insights into the subject-specific healing progression, and when used in combination with the
105 rtFE methods, it enables in vivo assessment and proportional changes to the loading conditions
106 simultaneously.

107

108 The objective of this study was to test the feasibility and effect of subject-specific adaptive mechanical
109 loading to treat bone defects. This was investigated in a newly developed mouse vertebral defect
110 model that allowed mechanical loading across the vertebrae, as well as high-resolution imaging for
111 rtFE analyses. As humans also share similarities to bone loading responses³¹, such a workflow could

112 pave the way for patient-specific loading regimes that increase the effect and repeatability of
113 mechanical loading regimes for bone regeneration strategies.

114

115 **Results**

116 **General observations**

117 All mice tolerated the defect surgery procedure well, with no impaired movement or indications of
118 pain, except one, which was euthanized out of precaution immediately after surgery due to perceived
119 excessive bleeding during surgery. None of the remaining mice experienced adverse effects from the
120 rtFE procedure, with no fractures or additional pain due to the workflow. One additional mouse was
121 euthanized after one week due to increasing and persistent swelling and signs of osteolysis in the
122 adjacent vertebrae around the pins. Furthermore, one defect was excluded from the data analysis
123 because it was drilled through two cortices. In total, this resulted in groups of 6 (control) and 7 (rtFE
124 loading) mice.

125

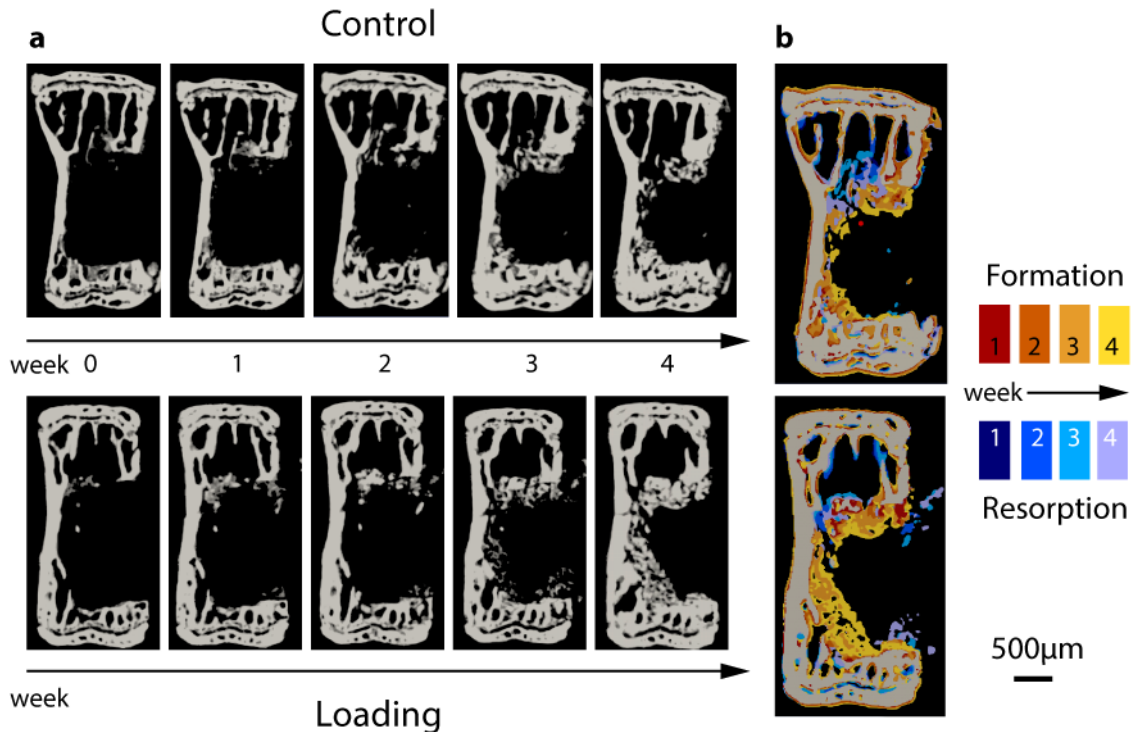
126 The rtFE method implemented in the study increased the total anesthesia time from approximately 22
127 minutes for the classic procedure to approximately 30 minutes. This additional time was due to the
128 computing time and adjustment of the loading device, and is a downside of the rtFE method
129 (Supplementary Fig. S3). No difference in the time to regain consciousness was noted, and all mice
130 recovered from the anesthesia as expected. Force increased significantly over time ($F(3,18)=25.8$,
131 $p<0.001$), with the initial average peak-to-peak force of the cyclic load calculated for the rtFE loading
132 groups was 4.3N (± 0.7), and significantly increased per week, first to 4.5 N (± 0.5), then to 4.8 N
133 (± 0.4), and to 5.2N (± 0.3) in the final week of loading.

134

135 Healing progressed appositionally from the ventral and lateral internal surfaces of the bone (Fig. 1a).

136 There were no signs of cortical bridging. Dense trabecular bone formed in regions where it would

137 bridge to adjacent surfaces (Fig. 1b), stabilizing the defect against the applied loading and consequent
138 bending moment induced by the defect asymmetry.

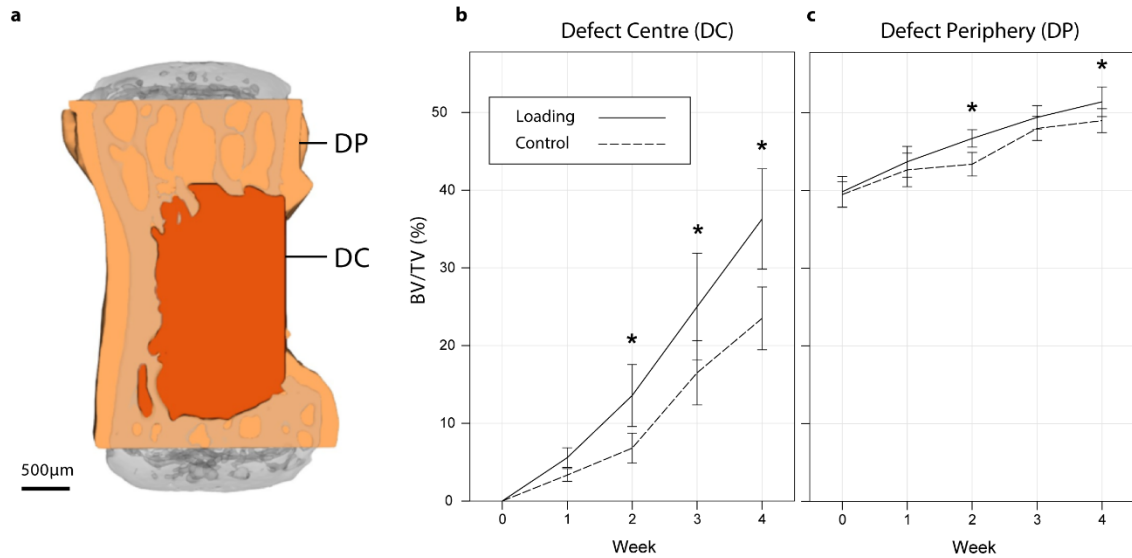


139
140 **Figure 1. Time lapsed imaging and overlay of formation and resorption on a weekly basis. (a)**
141 Time lapsed images of representative animals from both groups. **(b)** Weekly overlays show formation
142 and resorption patterns from 1 to 4 weeks post-surgery. Bone formed within the defect without cortical
143 bridging. Red/yellow: bone volume formed at week 1, 2, 3, and 4. Blue/purple: bone volume resorbed
144 at week 1, 2, 3, and 4.

145

146 Longitudinal assessment of bone defect healing

147 Two volumes were created to differentiate between the initial empty defect space, and the existing
148 surrounding bone. These were the defect centre (DC) and the defect periphery (DP). (Fig. 2a). Within
149 DC (Fig. 2b), a significant interaction was present for bone volume fraction (BV/TV) between time
150 and loading ($F(1,4)=8.90, p<0.005$). At week 2, 3 and 4, loading significantly increased BV/TV over
151 controls ($p<0.05$). BV/TV increased significantly over time in both loading and control groups
152 ($p<0.005$). In the DP, both time ($F(1,4)=164.7, p<0.005$) and the loading ($F(1,4)=5.34, p=0.041$) had
153 significant overall effects on BV/TV (Fig. 2c).

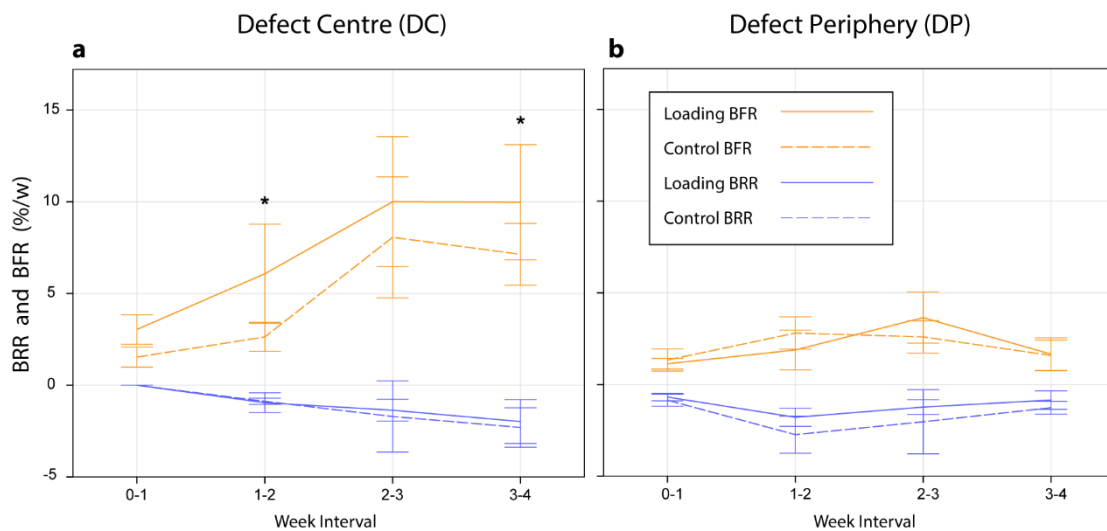


154

155 **Figure 2. Longitudinal changes in bone volume fraction. (a)** The vertebrae were divided into a
 156 defect centre (DC) and defect periphery (DP). **(b)** BV/TV within the DC significantly increased with
 157 the rtFE loading from week 2 compared to controls. **(c)** BV/TV within DP was also found to be
 158 influenced, but not to the same magnitude or extent as the DC.

159

160 Overall, loading ($F(1,3)=12.6$, $p<0.001$) and time ($F(1,3)=23.2$, $p<0.001$) had a significant effect on
 161 the DC bone formation rate (BFR/DC). Loading significantly increased BFR/DC over controls
 162 between weeks 1-2 ($F(1,3)=5.83$, $p=0.013$), and weeks 3-4 ($F(1,3)=4.39$, $p=0.042$), though did not
 163 reach significance for weeks 2-3 ($F(1,3)=2.05$, $p=0.159$) (Fig. 3a). Loading did not largely affect the
 164 DP bone formation rate (BFR/DP) or DP bone resorption rate (BRR/DP) at any time (Fig. 3b). Also,
 165 overall, loading did not have a large effect on BRR/DC or BRR/DP compared to control mice (Fig. 3).



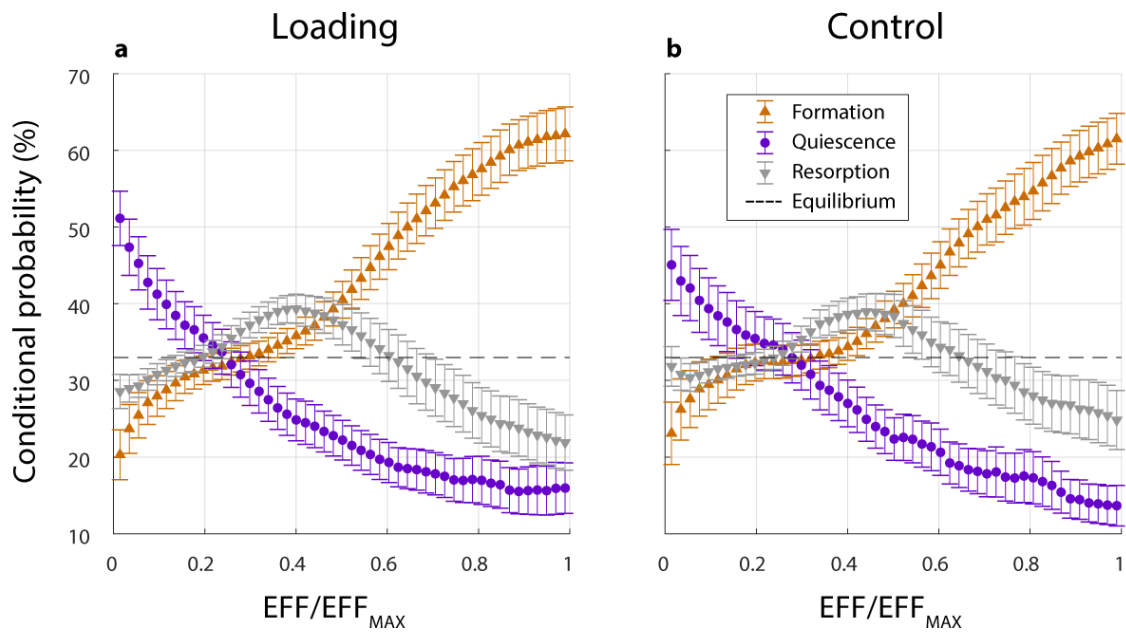
166

167 **Figure 3. Longitudinal changes in formation and resorption volume fractions. (a)** Loading
168 influenced the BFR/DC compared to controls, and reached significance at postoperative weeks 2 and
169 4, while loading did not appear to influence BRR/DC compared to controls. **(b)** Loading did not
170 significantly influence either BFR/DP or BRR/DP compared to controls, at any time interval.

171

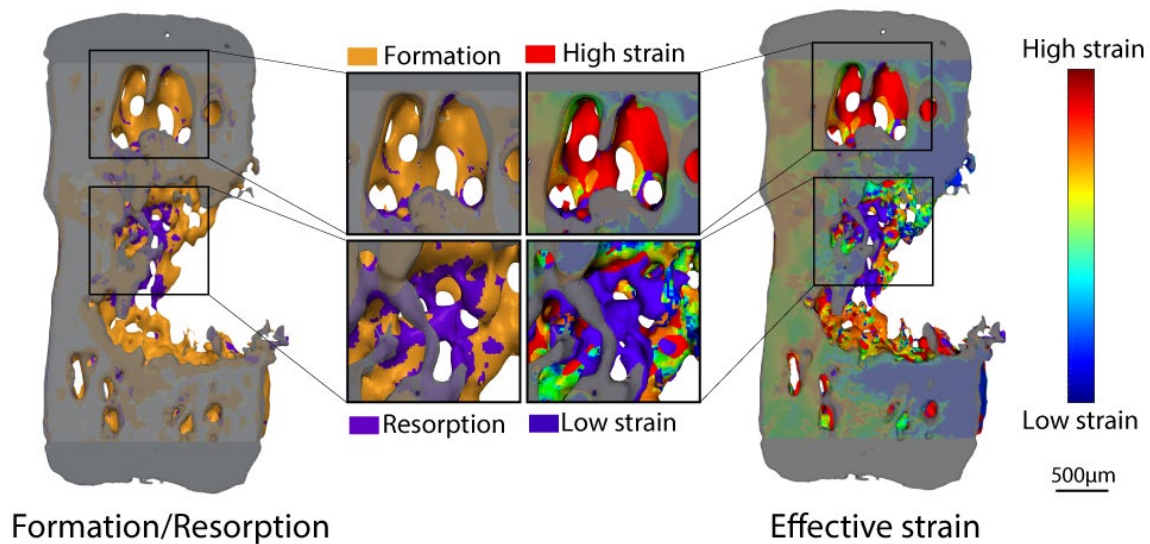
172 Mechanics of bone volume changes

173 After 4 weeks, none of the vertebrae had recovered their pre-surgery axial stiffness based on the
174 applied forces. From week 2 onwards, the treatment had a significant positive effect on FE-calculated
175 stiffness ($p < 0.05$, Supplementary Fig. S2a). There was also a significant positive Pearson's correlation
176 between BV/TV in the DC, and FE-calculated normalized stiffness ($r = 0.907$, $n = 51$, $p < 0.005$,
177 Supplementary Fig. S2b), while in the DP the correlation to normalized stiffness was significant, but
178 lower ($r = 0.809$, $n = 51$, $p < 0.005$). A pattern was noted in the probability of formation, quiescence, or
179 resorption events within the combined DC and DP regions; they were largely related to effective strain
180 (EFF). The effective strain as a percentile of the max effective strain (EFF/EFF_{MAX}) was used to find
181 the conditional probability of a (re)modelling event occurring due to strain. During the first week of
182 healing, bone formed with a random conditional probability ($cp(x) = 33.3\%$). However, in subsequent
183 weeks, bone formed in the upper half of the strain field ($cpF(x > 50\%) > 33.33\%$). The probability
184 for resorption was the highest within the first 30% of occurred strain leading to a small strain window
185 where bone was predominantly quiescent between 30% and 50% (Fig. 4a). This pattern also occurred
186 in control animals (Fig. 4b) where physiological strains were simulated with FE analysis (Fig. 5).
187 When comparing the loading and control cases, the curvature of the formation, resorption and
188 quiescence profiles in the loading cases had steeper and more pronounced curve sections compared to
189 the control cases. There was also a small shift towards lower EFF/EFF_{MAX} being formative with
190 loading.



191

192 **Figure 4. Conditional probabilities of formation and resorption events within the combined DC**
193 **and DP regions.** Effective strain as a ratio of the maximum effective strain value (EFF/EFF_{MAX}). (a)
194 Higher ratios of EFF/EFF_{MAX} led to formation activity in treatment groups, and lower ratios led to
195 resorption activity, regardless whether externally loaded in the treatment group, or in (b) control
196 animals with an assumed axial strain.



197

198 **Figure 5. Representative sample depicting formation and resorption relationship with effective**
199 **strain.** Regions of higher effective strain tended to formation, while lower effective strain tended to
200 resorption.

201

202 **Discussion**

203 While the influence of mechanical loading on bone (re)modelling is known, implementing this to
204 defect healing creates other challenges. These arise as two aspects, being the changed mechanical
205 environment due to the initial defect, and its unknown healing thereafter.

206

207 This study showed that by introducing an rtFE approach to an existing loading set-up²², bone defect
208 healing could be significantly improved over no-treatment controls. Importantly, this approach
209 succeeded in avoiding any incidence of fracture due to overloading, and in principle, homogenized
210 strain across different defect shapes, sizes, and healing progressions. Adaption of the loading within
211 the mechanical environment is not novel in itself, with mixed reports on the effectiveness of
212 dynamization^{12,32}, in which a change in stiffness of external fixators is adapted over healing periods.
213 Adding to these existing concepts, this study estimated individualized loads to apply during healing;
214 the rtFE approach allows much greater accuracy in the control of strain, as opposed to generic or pre-
215 determined adaptive regimes.

216

217 Loading started at two days after the defect was created, at which time the mice were still relatively
218 young at fourteen weeks old. The bone response to loading has previously been shown to have some
219 age-dependency on mice around this age, where six week old mice had a more exaggerated response
220 to loading compared to ten and sixteen week old mice³³. Hence, it could be questioned whether the
221 positive effect found in this study would also be repeated in older mouse. In this regard, it has been
222 reported that after sixteen weeks old, aging has less of an influence on the response to loading³⁰. At
223 fourteen weeks old, the mice in this study are near the border of this apparent age threshold. As such,
224 prior studies suggest the positive effect of this rtFE loading could be beneficial into adulthood and
225 beyond, though further studies would be needed to confirm this.

226

227 The timing of loading after bone injury is a topic of debate. In general, loading is known to influence
228 cell activity and function due to tissue deformation and fluid flow³⁴. Furthermore, it influences both
229 spatial and temporal biological responses at multiple scales^{35,36}. This aspect is more important in the
230 case of bone healing, where multiple overlapping phases exist. Early loading from two days onwards
231 has been reported less effective than delayed loading at two weeks³⁷. However, it has also been
232 reported that early cyclic loading may increase oxygen transport to the defect region³⁸, promoting the
233 longer term regeneration response. As differences in bone parameters were already noted after two
234 weeks in this study, it seems that early loading of three sessions per week is potentially more effective
235 than delayed loading, especially as subject-specific adaptive loading will be in an efficient range
236 without risking damage to early callus structures.

237

238 The new bone that formed within the defect did not appear to be simply recreating the pre-defect bone
239 structure, but to be forming based on other factors. During the defect healing, strain appeared to guide
240 bone (re)modelling activities, more so than an inherent sense of prior bone anatomy. Bone appeared to
241 form in compensation for the asymmetry of the defected bone, without cortical bridging, but with
242 densely arranged trabecular bone within the marrow cavity in a conical, V-like shape. This formation
243 pattern supports the idea of a universal cellular mechanobiological response regardless of the location
244 within the body, or the presence of fixation implants. This aligns with concepts of bone resorption
245 being caused by either disuse or stress-shielding, where the cells respond to the loads they experience
246 depending on their mechanical state, and not of the cause of the change. Further, the axial mechanical
247 stiffness over the four weeks, as assessed with FE, did not recover to its pre-defect strength,
248 suggesting that healing would continue into the future. The model was newly developed, and the level
249 of impairment over longer time periods would require further characterization of the model. As this
250 study duration was only four weeks, it is unclear whether (re)modelling would eventually result in a
251 structure similar to the native vertebra over time, or even have healed completely given more time.
252 Regardless, bone formation during early healing was related to and guided by bone strain (Fig. 5).
253 This applied to both the loaded and the control group, which could be exposed to physiological strain

254 that may peak at $4N^{14}$. Strain-induced bone (re)modelling principles have been previously
255 recognized^{15,16}, in which loading favors formation over resorption¹⁷.

256

257 This principle is evident elsewhere, where in a study of mouse femoral fractures, fracture site
258 remodeling after three weeks has shown to be consistent with previously considered remodeling
259 theories³⁹. However, such comparisons to other locations within the body can be confounded by non-
260 biomechanical factors. For example, the difference in the presence of bone marrow and stem cells,
261 cancellous and cortical bone ratios, and the large muscles surrounding the femur that supply blood and
262 cytokines. While different locations in the body have different factors that can influence healing,
263 similarities do exist between different bone defect models. This study developed and used a confined
264 partial defect model. When comparing this healing to an externally-fixated mouse femoral full
265 osteotomy defect model, mechanical loading from the fourth week onwards also significantly
266 increased BV/TV in the defect centre region. One difference though was the patterns in the BFR and
267 BRR once loading began¹⁹. Of relevance here is the phase of healing in which loading begins. In the
268 femoral full osteotomy model, a four week loading delay was implemented to allow for bridging
269 across the defect void. Thus, the inflammatory phase of healing has passed when loading begins. In
270 comparison, the partial vertebral defect used in this study allows for loading within the first week after
271 defect creation, during the early inflammatory phase of healing. When comparing healing in the
272 controls in the weeks following defect creation, the BFR and BRR showed similarities in responses
273 between both the osteotomy and partial defect models. It is clear that many confounding factors exist
274 when making such comparisons, including the timing of loading, the healing phase which loading
275 begins, the anatomical location and defect differences. Despite these differences, the bone healing
276 responses to loading within the defect centre and periphery were comparable between these very
277 different defect types. Overall, this further supports a universal relationship between bone healing and
278 loading in mice. Future experiments could confirm this by extending the timeline of loading past four
279 weeks in this vertebral model, by starting loading in later weeks, or by creating a full osteotomy
280 variation of this partial defect vertebral model. Comparisons to intact vertebrae also support the
281 relationship between healing and loading. The conditional probabilities of formation, quiescence and

282 resorption (Fig. 4) in this defect study correlate with prior studies of intact vertebra, where
283 (re)modelling events have a relationship to the strain percentile, and that loading may slightly shift the
284 strain percentile in which formation events occur^{15,25}. Considering the above studies, this rtFE study
285 also supports these mechanoregulation theories and further validates the principle in mouse vertebral
286 bone defect healing as well.

287

288 Over 80% of the variance ($r=0.907$, $R^2=0.823$) in BV/TV could be accounted for by change in FE-
289 calculated normalized stiffness, and this demonstrates the rtFE approach's ability to estimate the
290 loading intensity that should be applied. This provided some validation of the rtFE methods used. The
291 FE method, however, only accounted for purely axial compression, aligned to the principal component
292 of the vertebra. In reality, the vertebra was able to vibrate in different modes as it would be
293 constrained differently to the FE models. Therefore, it would have inevitably had some external
294 bending and rotational components not factored in by the simplified FE analyses. Despite this, the
295 relatively high correlation provides suitable confidence in the rtFE protocol. It kept the actual
296 computational processing time to around two minutes, to avoid the well-known effects of animal
297 anesthesia and its possibility to confound the results⁴⁰. Additionally, this correlation is noteworthy
298 considering a dynamic in vivo load was simplified to a static linear simulation. Such linear simulations
299 have previously been reported to be appropriate⁴¹ and capture this dynamic behavior via a static
300 apparent modulus⁴². Meanwhile, future improvements to computational non-linear analyses may
301 provide future insights⁴³. Overall, while assumptions and simplifications exist, this approach was able
302 to balance computational accuracy and cost, and provide confirmation of the usefulness of the rtFE
303 method.

304

305 This study did not compare subject-specific adaptive loading group to any traditional, non-adaptive,
306 non-subject-specific loading group. Mechanical loading is well-established to enhance bone healing,
307 and this has been extensively demonstrated in a variety of animal models using various loading
308 modalities. But many questions remain on how to implement this knowledge into practice, where

309 defects and their healing progression can vary widely. This study developed and implemented an
310 objective 3-dimensional imaging and analysis method to assess a defect and its healing, and
311 demonstrated how this could be linked to a known effective loading regime while reducing secondary
312 fracture risks (Supplementary Fig. S1). This overall approach attempts to foresee technological
313 progress and tools that could be more reliable than, for example, subjective grading scales of fractures
314 based on 2-dimensional imaging with subsequent loading based on this assigned grading scale. In this
315 regard, this study does not provide evidence that the complex, objective methodology presented in this
316 study provides improved outcomes compared to a simpler subjective analysis and/or non-adaptive
317 loading regime. Future studies could be designed to investigate if such a benefit truly exists between
318 these approaches. In principle, though, a leaning towards objective, (semi-)quantitative analyses have
319 historically prevailed over subjective, qualitative analyses, and this study attempts to follow this path.

320

321 As discussed, assumptions and simplifications created several limitations to this study which cover
322 both animal and computational aspects. For the animal aspects, the mice were relatively young, the
323 healing was not completed within the four weeks, and three mice were excluded which reduced study
324 power. Defects were created using relatively basic tools, and while this provides simplicity and an
325 ability to apply the model, it also introduces some variability in the defect volume across animals.
326 However, this is factored for in the BV/TV calculation. The pinning of the adjacent vertebra also
327 lacked certain control in position and angle, which creates unknowns in how the defect vertebra is
328 loaded, and the modes it vibrates in considering the semi-constrained nature. Future studies could be
329 extended past four weeks in older mice, improve the defect precision and repeatability, and increase
330 pinning control. As for the computational aspects, one of the greatest limitations is the simplifications
331 in the FE model. Firstly, the materials and models are linear elastic, which would not capture any non-
332 linear behaviour of vibration or visco-elastic effects. Material properties of the modelled discs were
333 that of bone, and all surrounding and void voxels not designated as bone were assigned a Young's
334 modulus of 3MPa, including what would be muscle or air. As such, both the disc and non-bone
335 regions are therefore stiffer than reality. Many of these computational limitations relate to the micro-
336 FE solver, ParOSol⁴⁴; however, these compromises enabled the efficient use of running the FE

337 remotely on a supercomputer, which created the possibility for near real-time results. While
338 computational power is itself a limitation, future studies could explore methods to more accurately
339 model such a dynamic system, and further validate the simplifications and assumptions used.

340

341 To translate this approach to patients, not only would further research and development be needed, but
342 for technological advancements also to continue. Most obviously, the computational and hardware
343 technology used in this study is not currently available to clinicians. Secondly, any patient-specific
344 solutions within the FE-realm require computational assumptions to be made, which requires further
345 expertise when applying case-by-case. These current limitations in translatability will likely be
346 overcome as technology develops; this study demonstrates the possibilities the future research can
347 strive towards, once technology and methods inevitably catch up for use in the larger-scales needed for
348 humans.

349

350 In conclusion, individualized real-time adaptive loading can be achieved through a combination of
351 micro-CT imaging, followed immediately by FE-solved strain distribution, and finally rescaling and
352 application of a cyclic loading force accordingly. Further investigation is needed to compare this to
353 traditional non-adaptive methods. This rtFE approach is highly relevant for clinical scenarios where
354 bone fractures and their healing progression are unique. This approach optimizes loading intensity,
355 and has the potential to reduce the risk of re-fracture or ineffective mechanical loading, thus improving
356 the healing of bone defects.

357

358 **Materials and Methods**

359 **Study design and surgery**

360 Approval was obtained for the animal experiments from the cantonal ethics committee from the
361 Kantonales Veterinäramt Zurich (Zurich, Switzerland, ZH029/18) prior to the study, and all
362 experiments were performed in accordance with Swiss animal welfare act and ordinance, and

363 ARRIVE guidelines. The study included two groups: an rtFE loading group, that were adaptively
364 loaded (3.2-5.5N, 10Hz, 5 minutes, 3000 cycles), and; a control group, that received sham loading
365 (0N) and similar handling. Groups were allocated by block randomization within a larger study, with
366 sample sizes estimated from previous similar research within the laboratory¹⁵, in which 2 groups for a
367 repeated (4) measures ANOVA using G*Power ($\beta=0.8$, $\alpha=0.05$, $f=0.7$, number measurements=4,
368 correlation=0.8) estimated a total sample size of 16 (n=8 per group). All surgical, scanning and
369 loading procedures were performed under isoflurane anesthesia (induction 5%, maintenance 1-2%, in
370 O₂). To be able to apply loading, three weeks prior to defect surgery, stainless steel pins (Fine Science
371 Tools, Heidelberg, Germany) were inserted in the fifth and seventh caudal vertebrae under
372 fluoroscopic control, as previously described (4). Perioperative analgesia (25 mg/L, Tramal,
373 Gruenthal GmbH, Aachen, Germany) was delivered via the drinking water for pre-emptive pain
374 relief two days prior to the defect surgery, and for three days post-surgery. All surgeries were
375 performed by the same surgeon. For both groups, defects of approximately 0.8mm x 1.5mm were
376 placed on the dorsal surface of the sixth caudal vertebrae of female fourteen-week old C57Bl/6JRj
377 (Janvier Labs, Saint-Berthevin, France) mice using an electric rotary drill (Micro Drill, Harvard
378 Apparatus, Holliston MA, United States) with 0.6mm and 0.8mm burs. This created an elongated void
379 running along the dorsal aspect of the vertebrae (Supplementary Fig. S3). Humane endpoints included
380 fracture, infection, bodyweight loss of > 15%, or inability to freely eat or drink.

381

382 Imaging and finite element methods

383 Vertebral defects were scanned at 10.5 μm resolution on the day of surgery, and weekly thereafter,
384 using an in vivo micro-CT (vivaCT 40, Scanco Medical AG, Brüttisellen, Switzerland, 55 kVp, 350
385 ms integration time, and 145 μA). The resulting images were used as input for the rtFE procedure for
386 animals in the loading group. Loading mice were kept under anesthesia during the image
387 reconstruction and FE calculation.

388

389 The reconstructed images were Gaussian filtered (sigma 1.2, support 1) to reduce noise, and
390 thresholded to assign material properties. Voxels within the threshold range from 395 mgHA/cm³ to
391 745 mgHA/cm³ were regarded as bone. This bone was assigned isotropic linear elastic material
392 properties with a Young's modulus between 4 GPa and 12.8 GPa, in threshold steps of 25 mgHA/cm³,
393 in proportion with their density⁴⁵. The Young's modulus of soft tissue was set to 3 MPa for values
394 lower than 395 mgHA/cm³. The Poisson's ratio was set to 0.3. Vertebra geometry was aligned to the
395 principal axis of the coordinate system in the z-direction. To achieve an even force distribution across
396 the bone and to counter numerical issues with the solver, discs of 1.68 mm diameter with a Young's
397 modulus of 12.8 GPa were added at the distal and proximal ends of the vertebrae, similar to previously
398 used¹⁷. The outer surface of the distal disc was fixated using Dirichlet boundary conditions. The outer
399 surface of the proximal disc was deformed by 1% by applying a pure compressive force in the normal
400 (z) direction. Each model was solved using the ParOSol solver⁴⁴, running at the Swiss National
401 Supercomputing Centre (CSCS, Lugano, Switzerland) with 64 CPUs, taking less than 2 minutes in
402 computing time. Effective strain was used as the output measurement for its ability to capture
403 inhomogeneity in newly formed bone tissue. The dynamic character of the loading was not considered,
404 in alignment with previous studies reporting that static simulations capture the main features and
405 evolution of the mechanical environment⁴¹, while keeping computational complexity and time down.

406

407 To calculate the rescaled force suitable for the individual defect and healing progression, strain
408 distributions were rescaled with a model intact vertebra with an 8N loading force used as the
409 reference³⁰. The 93rd percentile of strain resulting from the linear elastic FE model was used to rescale
410 the loading force from 1% deformation to the intact reference strain level. It is accepted that the strain
411 window most effective for bone modeling is between 800 and 2000 micro-strain²¹. Further, bone fails
412 when 1 – 7% of the tissue units within the volume exceed 7000 micro strain⁴⁶. To ensure that the
413 strain distribution in the defect model satisfies both requirements, the 99th percentile of strain derived
414 from five normal intact vertebrae of mice at similar age was used as a reference, and strain distribution
415 in the defect vertebrae down-scaled by this factor (ratio=93rd Defect/99th Intact, Supplementary Fig.
416 1b). This rescaled force was individual to each mouse and adjusted after imaging (Supplementary Fig.

417 S3), in what is termed real-time, as the bone is relatively unchanged during this period of scanning and
418 computation.

419

420 Animal model and loading

421 The first loading was applied two days after defect surgery, and three times per week thereafter. The
422 defect vertebra was loaded via the pins in adjacent vertebrae using an in-house cyclic loading device,
423 at 10Hz and 3000 cycles (5 minutes), similarly to previously reported¹⁵. The rescaled force calculated
424 from the rtFE pipeline was used until the following weekly scan was completed, to balance the
425 radiation exposure from imaging and the accuracy of the rescaled force. The rescaled force
426 corresponded to the peak-to-peak cyclic loading, with 0.5N being the base position of the lower peak
427 to avoid any inadvertent negative loads. Control mice were handled in a similar manner, and placed in
428 the loading device immediately after their scan for 5 minutes without any loading applied. The control
429 mice did not undergo the wait time associated with the rtFE computation.

430

431 Analysis of bone defect healing

432 For evaluation, two regions of interest were defined from the baseline defect scan of each animal (Fig.
433 1a). The defect centre (DC) included the bony surface surrounding the defect (1 layer of voxels) as
434 well as the space inside the defect. Region of interest determination was automated using a Hough
435 transformation feature extraction technique by overfitting a cylinder to the medullary cavity and
436 subsequently excluding any volume considered as existing bone within the created DC region. The
437 defect periphery (DP) covered the remaining bone volume up to the start of the growth plates, as well
438 as a dilated offset of 10 voxels to capture bone formation outside of the baseline cortical bone (Fig.
439 1a).

440

441 Bone volume fraction (BV/TV) was calculated in the DC (BV_{DC}/TV_{DC}) and in the DP (BV_{DP}/TV_{DP})
442 and normalized to their initial total volumes per region and per animal to calculate percentages⁴⁷.

443 Dynamic bone morphometric parameters were calculated in the DC and DP regions by registering
444 binary micro-CT images acquired at consecutive weeks which were overlaid to compute regions of
445 formation (F), quiescence (Q) and resorption (R) that could be analyzed morphometrically to yield
446 bone formation rate (BFR) and bone resorption rate (BRR)^{16,17} in the DC (BFR_{DC} and BRR_{DC}) and in
447 the DP (BFR_{DP} and BRR_{DP}), which is normalized to the respective initial volume, to calculate
448 percentages per week, as shown previously⁴⁸.

449
450 After registration, images were gauss-filtered ($\sigma = 1.2$, support 1) and thresholded to a binary image at
451 395mgHA/cm³ (corresponding to 4 GPa). Effective strain relevant to the (re)modelling events on the
452 bone surface was estimated using FE analysis as per the rtFE solving pipeline. By combing surface
453 (re)modelling events with corresponding surface effective strains, correlations and conditional
454 probabilities could be investigated in the DC and DP, similarly to previously reported¹⁵.

455
456 Linear mixed-effects modelling was used for the statistical analysis (SPSS 24.0.0.0). Fixed-effects
457 were allocated to: the time; and treatment. Random-effects were allocated to: the animal, to account
458 for the natural differences in healing between different mice; and the animals' specific defect volumes.
459 Assumptions were tested by analyzing the residuals of the fitted model. Post-hoc tests with multiple
460 pairwise comparisons were corrected with Bonferroni criteria. Data is reported as mean (\pm SD), unless
461 otherwise stated. Reporting of statistics follows guidelines from the Publication Manual of the
462 American Psychological Association (APA). A p-value of $p < 0.05$ was considered statistically
463 significant unless reported otherwise.

464

465 **Data availability**

466 All necessary data generated or analyzed during the present study are included in this published article
467 and its Supplementary Information files (preprint available on bioRxiv 2020.09.13.295402; doi:

468 <https://doi.org/10.1101/2020.09.13.295402>). Additional information related to this paper may be
469 requested from the authors.

470

471 **References**

- 472 1. Myeroff, C. & Archdeacon, M. Autogenous bone graft: Donor sites and techniques. *Journal of*
473 *Bone and Joint Surgery - Series A* (2011) doi:10.2106/JBJS.J.01513.
- 474 2. Goodship, A. E. & Kenwright, J. The influence of induced micromovement upon the healing of
475 experimental tibial fractures. *J. Bone Joint Surg. Br.* **67**, 650–5 (1985).
- 476 3. Schell, H. *et al.* The course of bone healing is influenced by the initial shear fixation stability.
477 *J. Orthop. Res.* (2005) doi:10.1016/j.orthres.2005.03.005.
- 478 4. Epari, D. R., Kassi, J. P., Schell, H. & Duda, G. N. Timely fracture-healing requires
479 optimization of axial fixation stability. *J. Bone Jt. Surg. - Ser. A* (2007)
480 doi:10.2106/JBJS.F.00247.
- 481 5. Betts, D. C. & Müller, R. Mechanical regulation of bone regeneration: Theories, models, and
482 experiments. *Frontiers in Endocrinology* (2014) doi:10.3389/fendo.2014.00211.
- 483 6. Meakin, L. B., Price, J. S. & Lanyon, L. E. The contribution of experimental in vivo models to
484 understanding the mechanisms of adaptation to mechanical loading in bone. *Frontiers in*
485 *Endocrinology* (2014) doi:10.3389/fendo.2014.00154.
- 486 7. Warden, S. J. & Turner, C. H. Mechanotransduction in the cortical bone is most efficient at
487 loading frequencies of 5-10 Hz. *Bone* (2004) doi:10.1016/j.bone.2003.11.011.
- 488 8. Yang, H., Embry, R. E. & Main, R. P. Effects of loading duration and short rest insertion on
489 cancellous and cortical bone adaptation in the mouse tibia. *PLoS One* (2017)
490 doi:10.1371/journal.pone.0169519.
- 491 9. Salisbury Palomares, K. T. *et al.* Mechanical stimulation alters tissue differentiation and
492 molecular expression during bone healing. *J. Orthop. Res.* (2009) doi:10.1002/jor.20863.
- 493 10. Thompson, Z., Miclau, T., Hu, D. & Helms, J. A. A model for intramembranous ossification
494 during fracture healing. *J. Orthop. Res.* (2002) doi:10.1016/S0736-0266(02)00017-7.
- 495 11. Augat, P., Merk, J., Wolf, S. & Claes, L. Mechanical stimulation by external application of
496 cyclic tensile strains does not effectively enhance bone healing. *J. Orthop. Trauma* (2001)
497 doi:10.1097/00005131-200101000-00010.
- 498 12. Claes, L. *et al.* Early dynamization by reduced fixation stiffness does not improve fracture
499 healing in a rat femoral osteotomy model. *J. Orthop. Res.* (2009) doi:10.1002/jor.20712.
- 500 13. Claes, L. *et al.* Late Dynamization by Reduced Fixation Stiffness Enhances Fracture Healing in
501 a Rat Femoral Osteotomy Model. *J. Orthop. Trauma* (2011)
502 doi:10.1097/BOT.0b013e3181e3d994.
- 503 14. Christen, P., Van Rietbergen, B., Lambers, F. M., Müller, R. & Ito, K. Bone morphology
504 allows estimation of loading history in a murine model of bone adaptation. *Biomech. Model.*
505 *Mechanobiol.* (2012) doi:10.1007/s10237-011-0327-x.
- 506 15. Schulte, F. A. *et al.* Local Mechanical Stimuli Regulate Bone Formation and Resorption in
507 Mice at the Tissue Level. *PLoS One* (2013) doi:10.1371/journal.pone.0062172.
- 508 16. Schulte, F. A., Lambers, F. M., Kuhn, G. & Müller, R. In vivo micro-computed tomography
509 allows direct three-dimensional quantification of both bone formation and bone resorption

- 510 parameters using time-lapsed imaging. *Bone* (2011) doi:10.1016/j.bone.2010.10.007.
- 511 17. Lambers, F. M., Schulte, F. A., Kuhn, G., Webster, D. J. & Müller, R. Mouse tail vertebrae
512 adapt to cyclic mechanical loading by increasing bone formation rate and decreasing bone
513 resorption rate as shown by time-lapsed in vivo imaging of dynamic bone morphometry. *Bone*
514 (2011) doi:10.1016/j.bone.2011.08.035.
- 515 18. Christen, P. & Müller, R. In vivo Visualisation and Quantification of Bone Resorption and
516 Bone Formation from Time-Lapse Imaging. *Current Osteoporosis Reports* (2017)
517 doi:10.1007/s11914-017-0372-1.
- 518 19. Wehrle, E., Paul, G. R., né Betts, D. C. T., Kuhn, G. A. & Müller, R. Individualized cyclic
519 mechanical loading improves callus properties during the remodelling phase of fracture healing
520 in mice as assessed from time-lapsed in vivo imaging. *bioRxiv* 2020.09.15.297861 (2020)
521 doi:10.1101/2020.09.15.297861.
- 522 20. Paul, G. R., Wehrle, E., Tourolle, D. C., Kuhn, G. A. & Müller, R. Reducing variance in a
523 mouse defect healing model: Real-time Finite Element Analysis allows homogenization of
524 tissue scale strains. *bioRxiv* 2020.09.02.274878 (2020) doi:10.1101/2020.09.02.274878.
- 525 21. Frost, H. M. A determinant of bone architecture. The minimum effective strain. *Clin. Orthop.*
526 *Relat. Res.* (1983) doi:10.1097/00003086-198305000-00047.
- 527 22. Webster, D. J., Morley, P. L., van Lenthe, H. H. & Müller, R. A novel in vivo mouse model for
528 mechanically stimulated bone adaptation - A combined experimental and computational
529 validation study. *Comput. Methods Biomech. Biomed. Engin.* (2008)
530 doi:10.1080/10255840802078014.
- 531 23. Webster, D. *et al.* Mechanical loading of mouse caudal vertebrae increases trabecular and
532 cortical bone mass-dependence on dose and genotype. *Biomech. Model. Mechanobiol.* (2010)
533 doi:10.1007/s10237-010-0210-1.
- 534 24. Webster, D., Wirth, A., Van Lenthe, G. H. & Müller, R. Experimental and finite element
535 analysis of the mouse caudal vertebrae loading model: Prediction of cortical and trabecular
536 bone adaptation. *Biomech. Model. Mechanobiol.* (2012) doi:10.1007/s10237-011-0305-3.
- 537 25. Scheuren, A. C. *et al.* Mechano-regulation of bone adaptation is controlled by the local in vivo
538 environment and logarithmically dependent on loading frequency. *bioRxiv* 2020.05.15.097998
539 (2020) doi:10.1101/2020.05.15.097998.
- 540 26. Harris, J. S., Bemenderfer, T. B., Wessel, A. R. & Kacena, M. A. A review of mouse critical
541 size defect models in weight bearing bones. *Bone* (2013) doi:10.1016/j.bone.2013.02.002.
- 542 27. Speirs, A. D., Heller, M. O., Duda, G. N. & Taylor, W. R. Physiologically based boundary
543 conditions in finite element modelling. *J. Biomech.* (2007)
544 doi:10.1016/j.jbiomech.2006.10.038.
- 545 28. Wehrle, E. *et al.* Evaluation of longitudinal time-lapsed in vivo micro-CT for monitoring
546 fracture healing in mouse femur defect models. *Sci. Rep.* (2019) doi:10.1038/s41598-019-
547 53822-x.
- 548 29. Tourolle né Betts, D. C. *et al.* The association between mineralised tissue formation and the
549 mechanical local in vivo environment: Time-lapsed quantification of a mouse defect healing
550 model. *Sci. Rep.* **10**, 1–10 (2020).
- 551 30. Lambers, F. M. *et al.* Bone adaptation to cyclic loading in murine caudal vertebrae is
552 maintained with age and directly correlated to the local micromechanical environment. *J.*
553 *Biomech.* (2015) doi:10.1016/j.jbiomech.2014.11.020.
- 554 31. Christen, P. *et al.* Bone remodelling in humans is load-driven but not lazy. *Nat. Commun.*
555 (2014) doi:10.1038/ncomms5855.

- 556 32. Glatt, V., Bartnikowski, N., Quirk, N., Schuetz, M. & Evans, C. Reverse dynamization
557 influence of fixator stiffness on the mode and efficiency of large-bone-defect healing at
558 different doses of rhBMP-2. *J. Bone Jt. Surg. - Am. Vol.* (2016) doi:10.2106/JBJS.15.01027.
- 559 33. Main, R. P., Lynch, M. E. & Van Der Meulen, M. C. H. Load-induced changes in bone
560 stiffness and cancellous and cortical bone mass following tibial compression diminish with age
561 in female mice. *J. Exp. Biol.* (2014) doi:10.1242/jeb.085522.
- 562 34. Vetsch, J. R., Betts, D. C., Müller, R. & Hofmann, S. Flow velocity-driven differentiation of
563 human mesenchymal stromal cells in silk fibroin scaffolds: A combined experimental and
564 computational approach. *PLoS One* (2017) doi:10.1371/journal.pone.0180781.
- 565 35. Glatt, V., Evans, C. H. & Tetsworth, K. A concert between biology and biomechanics: The
566 influence of the mechanical environment on bone healing. *Frontiers in Physiology* (2017)
567 doi:10.3389/fphys.2016.00678.
- 568 36. Paul, G. R., Malhotra, A. & Müller, R. Mechanical Stimuli in the Local In Vivo Environment
569 in Bone: Computational Approaches Linking Organ-Scale Loads to Cellular Signals. *Current*
570 *Osteoporosis Reports* (2018) doi:10.1007/s11914-018-0448-6.
- 571 37. Hausherr, T. C. *et al.* Effect of temporal onsets of mechanical loading on bone formation inside
572 a tissue engineering scaffold combined with cell therapy. *Bone Reports* (2018)
573 doi:10.1016/j.bonr.2018.04.008.
- 574 38. Witt, F., Duda, G. N., Bergmann, C. & Petersen, A. Cyclic mechanical loading enables solute
575 transport and oxygen supply in bone healing: An in vitro investigation. *Tissue Eng. - Part A*
576 (2014) doi:10.1089/ten.tea.2012.0678.
- 577 39. Isaksson, H. *et al.* Remodeling of fracture callus in mice is consistent with mechanical loading
578 and bone remodeling theory. *J. Orthop. Res.* (2009) doi:10.1002/jor.20725.
- 579 40. Balcombe, J. P., Barnard, N. D. & Sandusky, C. Laboratory routines cause animal stress.
580 *Contemp. Top. Lab. Anim. Sci.* (2004).
- 581 41. Huiskes, R., Rulmerman, R., Van Lenthe, G. H. & Janssen, J. D. Effects of mechanical forces
582 on maintenance and adaptation of form in trabecular bone. *Nature* (2000)
583 doi:10.1038/35015116.
- 584 42. Sarver, J. J. & Elliott, D. M. Mechanical differences between lumbar and tail discs in the
585 mouse. *J. Orthop. Res.* (2005) doi:10.1016/j.orthres.2004.04.010.
- 586 43. Sas, A., Ohs, N., Tanck, E. & van Lenthe, G. H. Nonlinear voxel-based finite element model
587 for strength assessment of healthy and metastatic proximal femurs. *Bone Reports* (2020)
588 doi:10.1016/j.bonr.2020.100263.
- 589 44. Flaig, C. A highly scalable memory efficient multigrid solver for μ -finite element analyses.
590 (2012). doi:10.3929/ethz-a-007613965.
- 591 45. Mulder, L., Koolstra, J. H., den Toonder, J. M. J. & van Eijden, T. M. G. J. Intratrabecular
592 distribution of tissue stiffness and mineralization in developing trabecular bone. *Bone* **41**, 256–
593 265 (2007).
- 594 46. Pistoia, W. *et al.* Estimation of distal radius failure load with micro-finite element analysis
595 models based on three-dimensional peripheral quantitative computed tomography images. *Bone*
596 (2002) doi:10.1016/S8756-3282(02)00736-6.
- 597 47. Bouxsein, M. L. *et al.* Guidelines for assessment of bone microstructure in rodents using
598 micro-computed tomography. *J. Bone Miner. Res.* **25**, 1468–1486 (2010).
- 599 48. Tourolle né Betts, D. C. *et al.* The association between mineralised tissue formation and the
600 mechanical local in vivo environment: Time-lapsed quantification of a mouse defect healing
601 model. *Sci. Rep.* (2020) doi:10.1038/s41598-020-57461-5.

602

603 **Acknowledgements**

604 The authors thank Nicholas Ohs, Duncan C. Tourolle for computational assistance, Ariane C.
605 Scheuren and Charlotte Roth for animal assistance, and the Swiss National Supercomputing Centre
606 (CSCS) for computational time. The authors thank Dr. Dr. Esther Wehrle for serving as deputy animal
607 study director for this project providing advice on study design, surgery training, and veterinary
608 support during the animal experiments. AM is also grateful for the funding from the William Harvey
609 International Translational Research Academy (WHRI-Academy, PCOFUND-GA-2013-608765), and
610 the European Commission under the Marie Curie Co-funding of Regional, National and International
611 Programmes (COFUND). The research leading to these results has received funding from the People's
612 Program (Marie Curie Actions) of the European Union's Seventh Framework Programme (FP7/2007-
613 2013) under REA grant agreement number 608765 This project also has received funding from the
614 European Research Council (ERC) under the FP7/2007-2013, entitled Advanced MechAGE, ERC-
615 2016-ADG-741883.

616

617

618 **Author Information**

619 **Affiliation**

620 Institute for Biomechanics, ETH Zurich, Zurich, Switzerland.

621 Angad Malhotra, Matthias Walle, Graeme R. Paul, Gisela A. Kuhn, Ralph Müller.

622

623 **Contributions**

624 The study was designed by AM, GAK, and RM. The computational rtFE aspects were developed by
625 AM, MW, and GRP, and performed remotely by MW. The animal experimental aspects were
626 developed and performed by AM and GAK. Statistical and data analyses were performed by AM and
627 MW. The manuscript was prepared by AM, and all authors reviewed and approved the final
628 manuscript.

629

630 **Additional Information**

631 **Competing interests statement**

632 The authors declare no competing interests.

633

634 **Figure Legends**

635 **Figure 1. Time lapsed imaging and overlay of formation and resorption on a weekly basis. (a)**
636 Time lapsed images of representative animals from both groups. **(b)** Weekly overlays show formation
637 and resorption patterns from 1 to 4 weeks post-surgery. Bone formed within the defect without cortical
638 bridging. Red/yellow: bone volume formed at week 1, 2, 3, and 4. Blue/purple: bone volume resorbed
639 at week 1, 2, 3, and 4.

640 **Figure 2. Longitudinal changes in bone volume fraction. (a)** The vertebrae were divided into a
641 defect centre (DC) and defect periphery (DP). **(b)** BV/TV within the DC significantly increased with
642 the rtFE loading from week 2 compared to controls. **(c)** BV/TV within DP was also found to be
643 influenced, but not to the same magnitude or extent as the DC.

644 **Figure 3. Longitudinal changes in formation and resorption volume fractions. (a)** Loading
645 influenced the BFR/DC compared to controls, and reached significance at postoperative weeks 2 and
646 4, while loading did not appear to influence BRR/DC compared to controls. **(b)** Loading did not
647 significantly influence either BFR/DP or BRR/DP compared to controls, at any time interval.

648 **Figure 4. Conditional probabilities of formation and resorption events within the combined DC**
649 **and DP regions.** Effective strain as a ratio of the maximum effective strain value (EFF/EFF_{MAX}). **(a)**
650 Higher ratios of EFF/EFF_{MAX} led to formation activity in treatment groups, and lower ratios led to
651 resorption activity, regardless whether externally loaded in the treatment group, or in **(b)** control
652 animals with an assumed axial strain.

653 **Figure 5. Representative sample depicting formation and resorption relationship with effective**
654 **strain.** Regions of higher effective strain tended to formation, while lower effective strain tended to
655 resorption.